



Ultrasonic-assisted synthesis of porous S-doped carbon nitride ribbons for photocatalytic reduction of CO₂

Jiabei Wang, Zhiqiang Jiang

School of Materials Science and Chemical Engineering, Ningbo University of Technology, 201 Fenghua Road, Jiangbei, Ningbo, Zhejiang, 315211, China

ARTICLE INFO

Keywords:

Graphitic carbon nitride
Sonochemical approach
Photocatalytic reduction
Electrochemical reaction

ABSTRACT

A series of porous S-doped carbon nitride ribbons (PSCN) were prepared by one-pot hydrothermal and sonochemical synthesis techniques. The morphologies and nanostructures of the catalysts were characterized by SEM, XRD and IR, which confirmed the pristine graphitic structures of carbon nitrides retained in the products. Due to sonication treatment, PSCN has porous structures in the thin ribbon and larger specific surface areas (PSCN 43.5 m²/g, SCN 26.6 m²/g and GCN 6.5 m²/g). XPS and elemental mappings verified that sulfur atoms were successfully introduced into the carbon nitride framework. Diffuse reflectance spectroscopy (DRS) results showed S-doping in the carbon nitride reduced the bandgap energy and enhanced their capability of the utilization of visible light, which contributed to higher photo-generated current. Photoluminescence (PL) analysis indicates the recombination of photogenerated carriers was suppressed in PSCN. Moreover, the photocatalytic performance showed that S-doping and porous and thin ribbon nanostructures may effectively boost the CO₂ reduction rate (to as much as 5.8 times of GCN) when illuminated by visible light (>420 nm) without the need of sacrificial materials. The preliminary mechanisms of the formation of PSCN and its applications in photocatalytic CO₂ reduction are proposed. It highlights the potential of the current technique to produce effective, nonmetal-doped carbon nitride photocatalysts.

1. Introduction

A key component of the atmosphere that affects both the carbon cycle and the climate of the planet is carbon dioxide (CO₂). The primary cause of climate change is generally agreed to be the rising level of atmospheric CO₂ brought on by the burning of fossil fuels [1]. Researchers have devised a variety of CO₂ reduction strategies, including thermochemical [2], electrochemical [3], and photochemical methods [4]. Methanol, carbon monoxide, ethylene, and other compounds can be produced from CO₂ [5–7] But the development of catalysts for CO₂ photo-reduction is still lagging due to a lack of effective, reliable, cost-effective, and highly selective catalysts.

Because of its inherent benefits, including a good band gap, environmental friendliness, affordability, and ease of production, carbon nitride is regarded as a promising photocatalyst [8,9]. Traditional graphitic carbon nitrides (GCN) made by direct calcination of precursors, on the other hand, are constantly constrained by their bulky structure, uncontrolled band gap, and rapid charge carrier recombination, which limits the active species and useful catalytic sites [10]. Several strategies have recently been devised to enhance the

performance of bare GCN, including doping with non-metal [11,12] or metal elements [13,14], as well as creating composites with other semiconductors [15,16]. However, when exposed to people and the environment, carbon nitrides that have been doped with metals like Zn, Cu, Pb, Ni, etc. produce an accumulation of their hydrated ions, which impacts public health and the environment [17,18]. As a result, there is an urgent need for an efficient non-metal-doped photocatalyst.

Graphitic carbon nitrides which were doped with non-metal elements like oxygen [19,20], nitrogen [21–23], carbon [24,25] and phosphorus [26,27], were reported to substitute the original atoms in the 2D carbon nitride framework and altered g-C₃N₄'s electronic structure. Sulfur-doped g-C₃N₄ prepared by treating the g-C₃N₄ powder in a gaseous H₂S atmosphere or by thermolysis of thiourea was demonstrated by Liu et al [28] and Wang et al [29]. S element substituted nitrogen in the aromatic tri-s-triazine rings, reduced recombination of photoinduced electrons and holes and enhanced its photoreactivity. In addition to elemental doping, structural modulation also plays a key role in catalyst design [30–32]. The geometry design of g-C₃N₄ allows to enhance scattering and reflection of the incident light, which would result in the significant advancement of light harvesting efficiency and

E-mail address: jiangzqiang@hotmail.com (Z. Jiang).

<https://doi.org/10.1016/j.ultsonch.2022.106273>

Received 25 October 2022; Received in revised form 6 December 2022; Accepted 19 December 2022

Available online 23 December 2022

1350-4177/© 2022 The Author(s). Published by Elsevier B.V. This is an open access article under the CC BY-NC-ND license (<http://creativecommons.org/licenses/by-nc-nd/4.0/>).

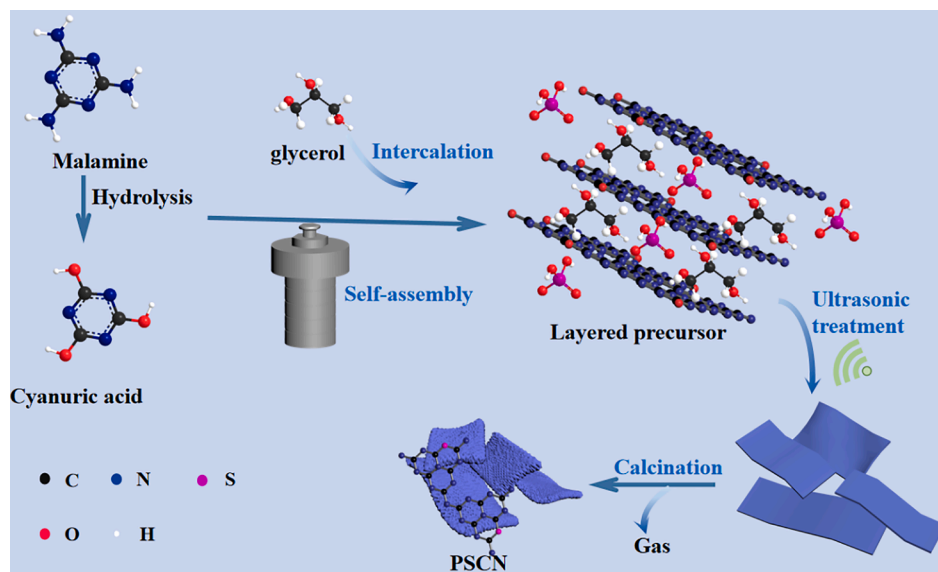


Fig. 1. Schematic diagram on the fabrication of PSCN photocatalyst.

improve its photoreactivity. In this research, we focus on the ultrasonication-aided synthesis of porous S-doped carbon nitride ribbons (PSCN) and its capability for CO₂ photocatalytic reduction under visible light radiation. Surprisingly, as-prepared catalysts greatly extended the absorption of visible light and promoted photocatalytic performance. Fig. 1 illustrates the synthesis of PSCN from melamine, sulfuric acid as the precursor by hydrothermal synthesis, followed by ultrasonication, and calcination. As a result, the photocatalyst possesses a porous nano-ribbon microstructure and showed a significantly enhanced photocatalytic CO₂ reduction rate (up to 30.3 μmol·g⁻¹·h⁻¹), which was 5.8 times that of GCN photocatalysts.

2. Experimental section

2.1. Materials

The chemical reagents used for the synthesis of PSCN were commercially available. Melamine (99 %, Aladdin, Shanghai, China), concentrated sulfuric acid (95.0–98.0 %, Aladdin, Shanghai, China), ethanol (≥99.8 %, Aladdin, Shanghai, China) and glycerol (≥99.5 %, Aladdin, Shanghai, China), sodium sulfate (Na₂SO₄, 99 %, Aladdin, Shanghai, China), and deionized water (Millipore, 18.2 MΩ cm) were used as chemical reagents without further purification.

2.2. Synthesis of catalysts

The catalyst PSCN was synthesized using a one-pot hydrothermal method. First, melamine (2 g) was dissolved in 60 ml glycerol to form a clear solution at 80 °C. 0.8 ml concentrated sulfuric acid was added and stirred for 15 min. Then, it was transferred into a Teflon-lined autoclave and heated at 150 °C for 12 h. After that, the slurry was obtained by filtrating the mixed solution. 20 ml ethanol and 20 ml deionized water was added to the slurry in a 100 ml glass cup and was ultrasonicated at 80 °C for 1 h. The mixture was filtered, and the precipitated solid was washed with ethanol and deionized water, followed by drying for 24 h at 80 °C in a vacuum oven. Finally, PSCN was obtained by calcinating the resulting solid at 550 °C for 2 h with a heating rate of 2 °C·min⁻¹. The sample synthesized using the same method but without ultrasonication was denoted as SCN. Additionally, the sample synthesized by directly calcining melamine at 550 °C for 2 h was denoted as GCN.

2.3. Characterization

XRD spectra were obtained using a Bruker D8 Advance diffractometer (Cu Kα radiation). An attenuated total reflection (ATR) configuration was used to gather the IR spectra using a Thermo Nicolet iS50 FTIR spectrometer. Field emission scanning electron microscopy (FESEM S-4800, Hitachi, Japan), was used to characterize the morphology characteristics of the sample products. Diffuse reflectance spectra (DRS) were recorded on a Varian Cary 4E UV–vis system with Labsphere diffuse reflectance accessory. Bandgap energy (E_g) of the GCN, SCN and PSCN samples was calculated according to the following formula:

$$(\alpha h\nu)^{1/n} = C(h\nu - E_g)$$

where α , ν , and C are the absorption coefficient of the materials, light frequency, and the constant, respectively. The parameter n is related to different electronic transitions ($n = 2$ for indirect-allowed and $n = 1/2$ for direct-allowed transitions, respectively). Photoluminescence (PL) spectra were acquired on a Fluorescence Spectrophotometer (F-7000, Hitachi, Japan) at an excitation wavelength of 380 nm. X-ray Photoelectron Spectroscopy (XPS) was carried out on Thermo ESCALAB 250 monochromatized Al Kα at $h\nu = 1486.6$ eV. Pore size distribution and the specific surface area of the materials were calculated by the BET model using nitrogen adsorption–desorption data at 77 K Micromeritics ASAP 2460, USA) in the pressure range of $P/P_0 = 0-1$.

2.4. Photoelectrochemical measurements

Photoelectrochemical measurements were performed on an electrochemical analyzer (CHI660E, CHI Shanghai, Inc.) using a standard three-electrode configuration with a Pt wire and Hg/Hg₂Cl₂ (in saturated KCl) as the counter electrode and reference electrode. The working electrode was prepared as follows: 5 mg of light ground GCN, SCN or, PSCN was mixed with 0.5 ml of alcohol to produce a slurry. The slurry was then evenly dispersed onto a fixed area (≈1 cm²) of an ITO glass substrate, followed by drying the ITO glass substrate electrode at 60 °C for 10 h.

2.5. Photoactivity performance

The photocatalytic CO₂ reduction test was performed on homemade equipment. A 300 W Xenon lamp with a 420 nm cutoff filter was used as the visible light source. The as-prepared photocatalyst (10 mg) was

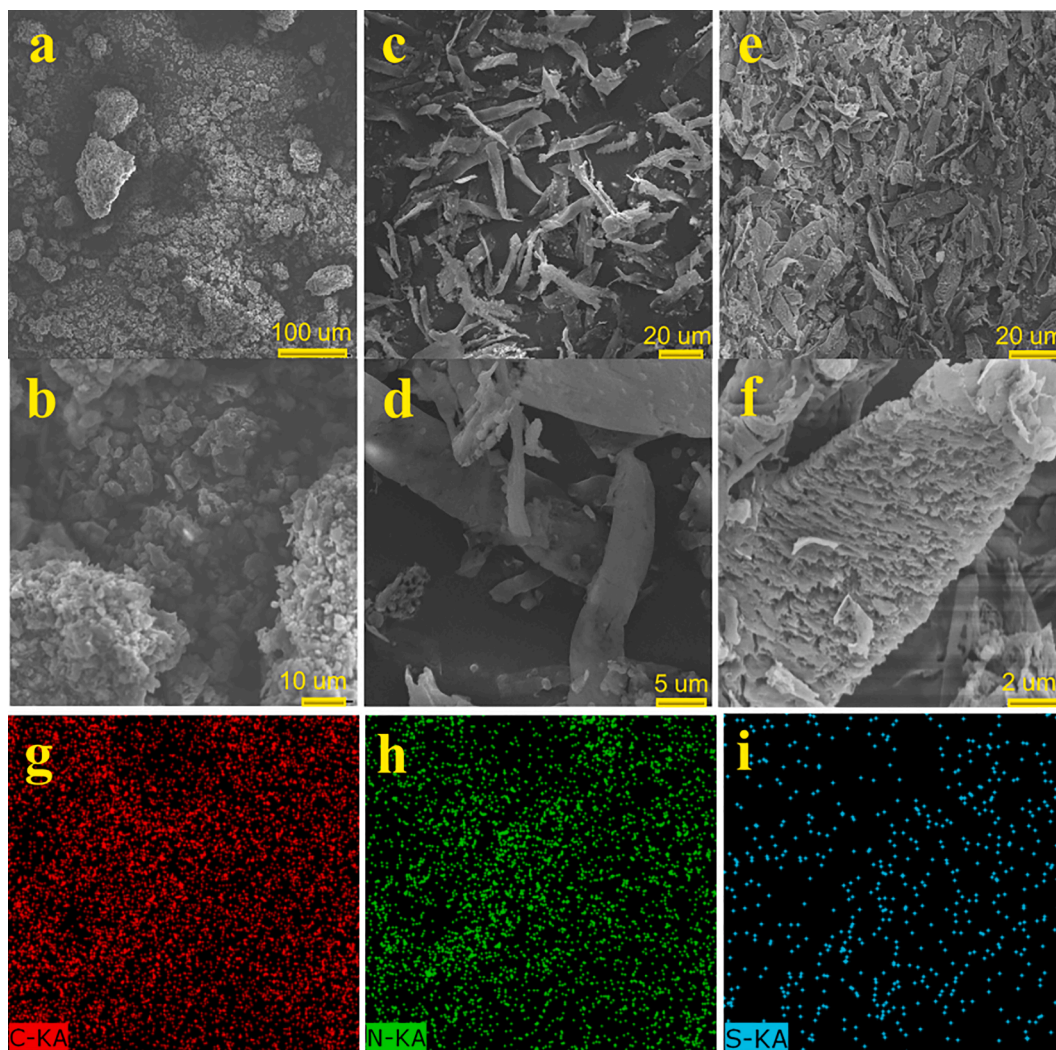


Fig. 2. SEM image of GCN (a, b), SCN(c, d), and PSCN(e, f), (a); Element mapping of C (g), N (h), and S (i) of PSCN.

suspended in 10 ml of deionized water in a 100 ml glass cup by ultrasonication. Then it was transferred into a 50 ml round-bottom quartz photo-reactor. The reactor was sealed with a silicone rubber septum and the solution was saturated with CO₂ gas for 30 min. After light irradiation for some time, the gaseous products such as CO, CH₄ were measured by gas chromatography.

3. Results and discussions

3.1. Synthetic strategy of PSCN

PSCN was synthesized by self-assembly of the protonated melamine in glycerol mediated with sulfuric acid, which polymerized and subsequently self-assembled to layer structures (Fig. 1). The glycerol molecules intercalated between the carbon nitride layers during the

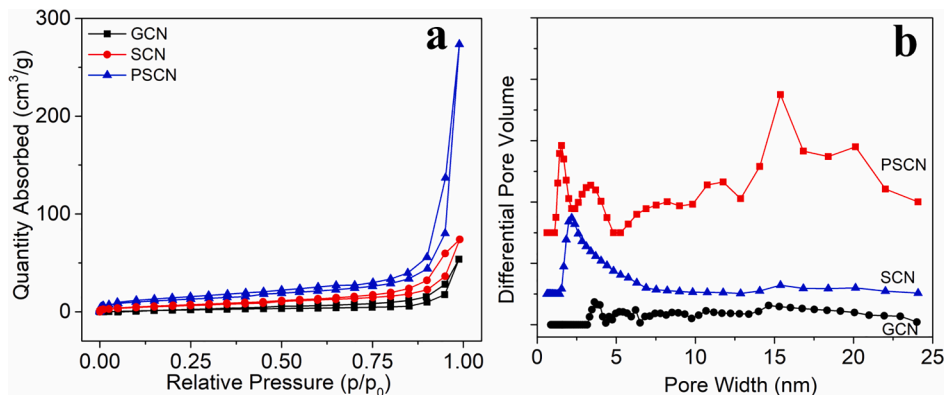


Fig. 3. Nitrogen adsorption – desorption isotherms (a) and pore size distribution (b) of GCN and PSCN.

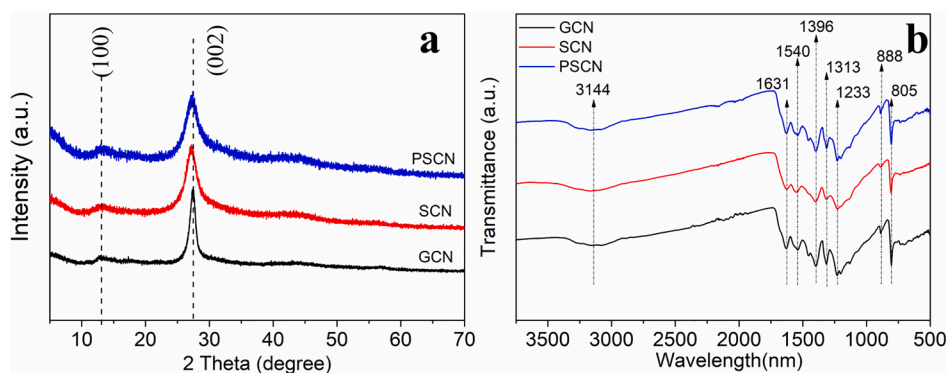


Fig. 4. XRD patterns (a) and FTIR spectra (b) of GCN, SCN, and PSCN.

hydrothermal process [33] and the ultrasonic exfoliation [34] during the washing step could contribute to the formation of the narrow ribbon. Meanwhile, the $-S-OH$ of sulphuric acid was carbonized with melamine to form $C-S$ bonds in the framework. Additionally, the precursor would shrink in bulk during the thermal calcination process, causing many pores to form on the layers, therefore generating a porous ribbon structure. The tentative formation mechanism was schematically illustrated in Fig. 1.

3.2. Catalyst microstructures

The SEM images of as-prepared GCN, SCN, and PSCN are shown in Fig. 2. GCN is bulky and lacks discernible pores (Fig. 1a–b), and its substantial agglomeration was primarily driven by heterogeneous heat transfer during condensation polymerization [35]. In contrast, S-doped carbon nitride samples, including SCN and PSCN, formed thin ribbons (Fig. 1b,e). With the aid of ultrasonic treatment, loose and porous structures with numerous randomly organized layers and edges were

formed in the ribbons of PSCN sample. These thin layer structures and porous channels can increase the light absorption, maximize reactive sites on the surface, and reduce carriers' recombination, all of which enhance the efficiency of the photocatalyst [36]. C, N, and S elements were observed in the PSCN catalyst, according to the EDS element mappings in Fig. 2g–i. The results indicated that the carbon nitride matrix has an even distribution of S elements.

BET surface areas and pore size distributions of GCN, SCN and PSCN were studied by analyzing the nitrogen adsorption–desorption isotherms of all the samples. The specific surface area of PSCN reached $43.5 \text{ m}^2/\text{g}$, which was larger than $26.6 \text{ m}^2/\text{g}$ of SCN and $6.5 \text{ m}^2/\text{g}$ of GCN. As seen in Fig. 3a, all the samples exhibit a type IV isotherm with a hysteresis loop of H1, which proves the presence of cylindrical mesopores in these materials [37]. The isotherms displayed a high absorption in the high relative pressure (P/P_0) region (from 0.9 to 1.0), suggesting the development of mesopores in the PSCN samples. In the pore size distribution curves of SCN and PSCN, a new peak at around 2.2 nm appeared, which may be attributed to the development of new pores by S

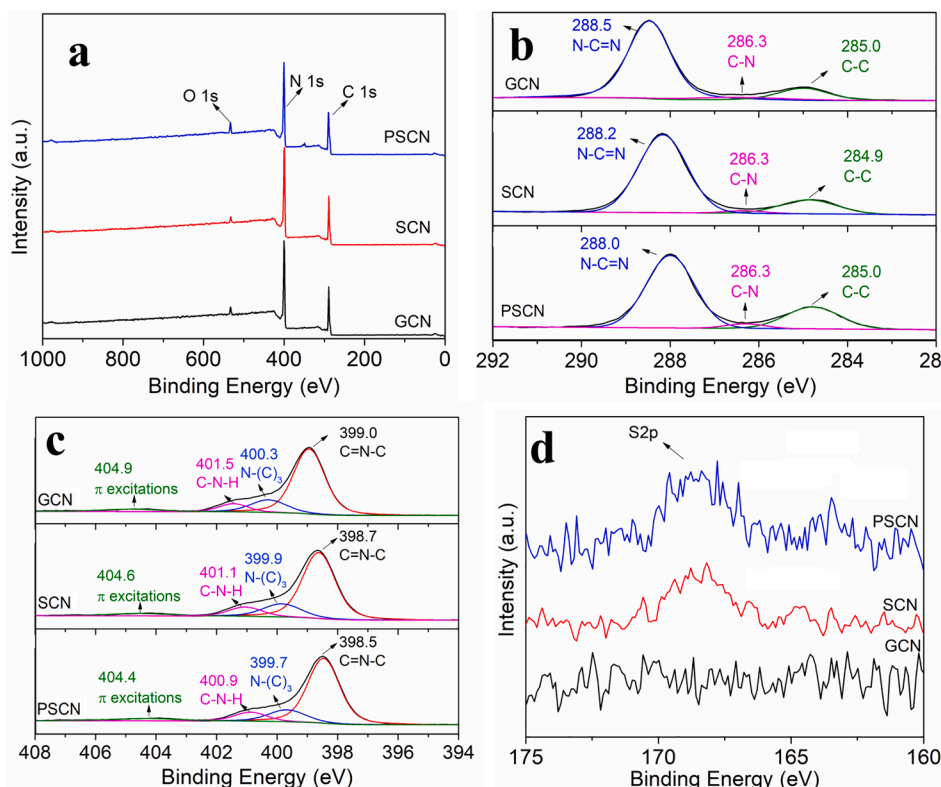


Fig. 5. XPS survey spectra (a), high-resolution C1s (b), N1s (c), and S2p (d) of GCN, SCN, and PSCN.

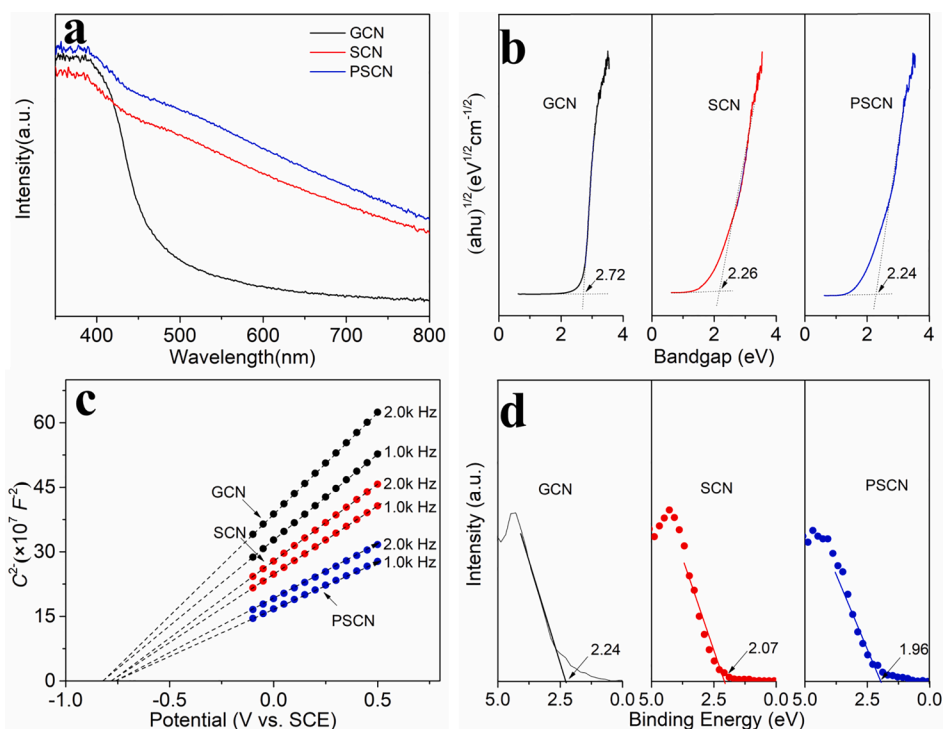


Fig. 6. UV – vis diffuse reflectance spectra (a), estimated band gaps (b), Mott – Schottky curves (c), and XPS-VB plot (d) of GCN, SCN, and PSCN.

doping. This result, in accordance with TEM analysis, proves that the incorporation of S element to GCN can produce more small pores in addition to the increased surface area. PSCN showed wider pore size distribution from 10 nm to 25 nm. As a result of greatly enhanced BET surface area and pore volume, more reaction sites can be formed on the surface of PSCN. Meanwhile, the porous structures can accelerate reactant diffusion, which contributes to photocatalytic activity.

The XRD patterns of samples in Fig. 4a showed similar diffraction peaks, suggesting that these three samples had similar crystal structures [38]. The XRD curves have two typical diffraction peaks at 13.0° and 27.4° , which are attributed to (100) and (002) crystal planes of carbon nitrides, respectively. The (100) plane was assigned to the in-plane structural packing of aromatic systems with an average distance of $d = 0.675 \text{ nm}$ [39]. The (002) plane was assigned to interlayer stacking of conjugated aromatic systems, corresponding to the average interlayer distance of $d = 0.326 \text{ nm}$ [40]. After modification, the diffraction peak shifted to 27.0° for SCN and PSCN. It was possibly caused by S atoms incorporated into the C–N framework led to more curved structures and an increase in layer spacing [41]. FTIR spectra (Fig. 4b) showed the bending vibration of tri-s-triazine units at 805 cm^{-1} and the stretching vibration of the aromatic C–N rings at $1230\text{--}1750 \text{ cm}^{-1}$. The peaks at $3000\text{--}3300 \text{ cm}^{-1}$ were assigned to the stretching vibration of the amino groups at the edge of the rings [42]. FTIR results of SCN and PSCN show similar patterns with GCN, suggesting that S-doping did not disrupt the original 2D conjugated structures of GCN.

The XPS technique was used to elucidate the chemical compositions and oxidation states of constituent elements in the GCN, SCN and PSCN samples. The XPS survey spectra (Fig. 5a) demonstrated the presence of C, N, and O elements with sharp peaks at 288 eV (C 1s), 400 eV (N 1s), and 532 eV (O 1s), but no noticeable peaks corresponding to S elements in the SCN and PSCN samples. This suggests low doping levels of sulfur in SCN and PSCN. The high-resolution XPS spectra of C, N, and S elements in GCN, SCN and PSCN samples are presented in Fig. 5b-d. In the C1s spectra of GCN, three peaks with binding energies of 288.5 eV, 286.3 eV, and 285.0 eV were observed. These peaks are assigned to the sp^2 hybrid C atoms in the aromatic ring ($\text{N}=\text{C}=\text{N}$), C atoms generated by partial condensation polymerization at the edge of the aromatic ring

(C–NH₂), and carbon impurity on the surface (C–C, C=C), respectively [43,44]. As shown in Fig. 5c, the peaks at 399.0, 400.3, and 401.5 eV are assigned to the N atoms in the aromatic C–N rings (C–N=C), the sp^3 hybridized structures (N–C₃), and at the end of aromatic rings (C–NH_x) [29,45], respectively. The weak peak at 404.9 eV is assigned to π excitations [46]. Fig. 5d shows the high-resolution spectra of S 2p. From the spectra, the atomic contents of the S element were calculated to be 0.75 wt% and 0.86 wt% in SCN and PSCN samples, respectively. The binding energy of S 2p in PSCN at around 168.5 eV was assigned to S–C bonds formed by replacing the N atoms with the S atoms [47]. Furthermore, for SCN and PSCN, similar patterns of C 1s and N 1s spectra without significant binding energy shifts were observed. It implies that the aromatic CN heterocycles in both samples have nearly identical chemical states for carbon and nitrogen.

3.3. Charge-carriers separation and transport

In Fig. 6a,b, UV–vis diffuse reflectance spectra and computed band gaps are displayed. The band gap of pure phase GCN has a value of around 2.72 eV, comparable to the graphitic carbon nitride reported in the literature [40]. After S element doping, SCN and PSCN's light absorption in the full spectrum (350–800 nm) was strengthened and revealed a clear redshift. The band gap values of SCN and PSCN are about 2.26 eV and 2.24 eV, respectively. Light absorption in the visible range plays a crucial role in photocatalytic performance. All the samples absorbed high-intensity ultra-violet light, but GCN showed a sharp edge at around 420 nm, while PSCN and SCN didn't show an obvious decrease and have a tail extending to near IR region. The red shift of the absorption wavelength indicated that PSCN and SCN can absorb more solar energy to produce more photogenerated electrons and holes pair. Fig. 6c shows the Mott–Schottky curves with the saturated calomel electrode (SCE) as the reference electrode. GCN, SCN, and PSCN all have positive fitting slopes, suggesting they are *n*-type semiconductors [48]. The flat band potentials of GCN, SCN, and PSCN are -0.82 , -0.78 , and -0.76 V , respectively. The Fermi levels (E_f) of GCN, SCN, and PSCN are -0.60 , -0.56 , and -0.54 V , respectively [49]. The XPS–VB spectra (Fig. 6d) showed that the band gaps of GCN, SCN, and PSCN between the Fermi

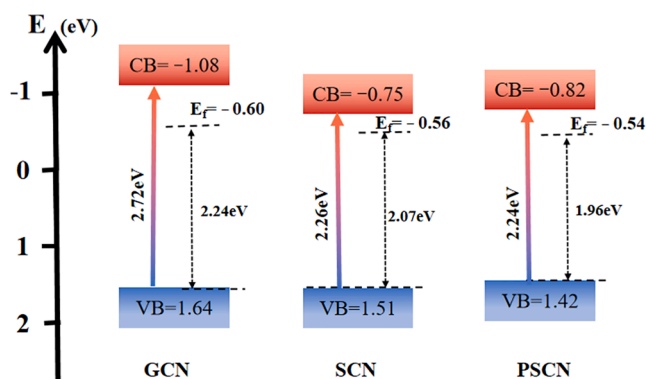


Fig. 7. Potential level and charge transport of GCN, SCN, and PSCN.

level and valence band (VB) are 2.24, 2.07, and 1.96 eV [50], respectively. The VB potentials are calculated to be 1.64, 1.51, and 1.42 eV for GCN, SCN, and PSCN, respectively, while the conduction bands (CB) are determined to be -1.08 , -0.75 , and -0.82 eV, respectively [51]. The potential changes of GCN, SCN, and PSCN are shown in Fig. 7, and the band gaps and electron migration in the samples are illustrated. From these results, S-doping is effective in both narrowing the bandgap and increasing VB width of C_3N_4 by the interaction of S 3p states with N 2p states, which justifies the appreciated photoactivity of the modified catalysts [28].

Fig. 8a presents the transient photocurrent responses of all the sample electrodes. The photocurrent density from the PSCN electrode reached the maximum, which was about 2.7 times that of GCN and 1.5 times that of SCN. Higher photocurrent value represents more efficient separation of electrons and holes. It shows that PSCN can produce more

electrons and obtain efficient visible light guidance. After many cycles, the transient photoinduced current from the PSCN electrode can respond continuously without noticeably decreasing, showing that the PSCN structure remained stable when exposed to visible light. The recombination and separation of photo-induced charge carriers are investigated using photoluminescence spectroscopy.

Fig. 8b shows the PL emission spectra under an excitation wavelength of 380 nm, and the peaks of the samples were centered at around 460 nm. It is known that the unshared pair of electrons of heterocyclic nitrogen 2p orbitals form HOMO and the sp^2 hybridized carbon-nitrogen clusters form LUMO. The emission with the peak at around 460 nm comes from the transition of electrons from the LUMO- π^* state to the HOMO-n state [52,53]. There is no significant peak shift can be observed, which implies the transition of electrons in these three samples follows the same mechanism. A lower peak intensity corresponds to a lower recombination rate of electrons and holes [31,54]. The PL intensity gradually decreases from GCN to PSCN indicating PSCN undergoes the most intense fluorescence quenching of all the samples, possibly due to the electrons generated by light irradiation being trapped in the defects. Since PSCN's peak is lower than those of SCN and GCN, PSCN has more free electrons, as confirmed by the photocurrent results, which can subsequently be transferred from the sample to the reactants for reduction of CO_2 .

3.4. Photocatalytic performance

Fig. 9 displays the CO yield rates for all samples during CO_2 reduction when illuminated by visible light. In comparison to GCN, the reduction rates of the S-doped catalysts (SCN and PSCN) were improved. PSCN has a rate of $30.3 \mu\text{mol}\cdot\text{h}^{-1}\cdot\text{g}^{-1}$, which is higher than GCN's ($5.2 \mu\text{mol}\cdot\text{h}^{-1}\cdot\text{g}^{-1}$) and SCN's ($20.1 \mu\text{mol}\cdot\text{h}^{-1}\cdot\text{g}^{-1}$) by around 5.8 times

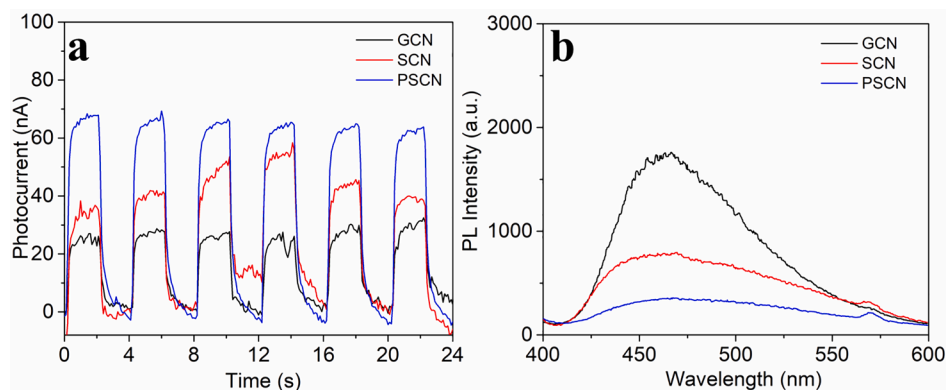


Fig. 8. Transient photocurrent responses (a) and PL spectra (b) of GCN, SCN and PSCN.

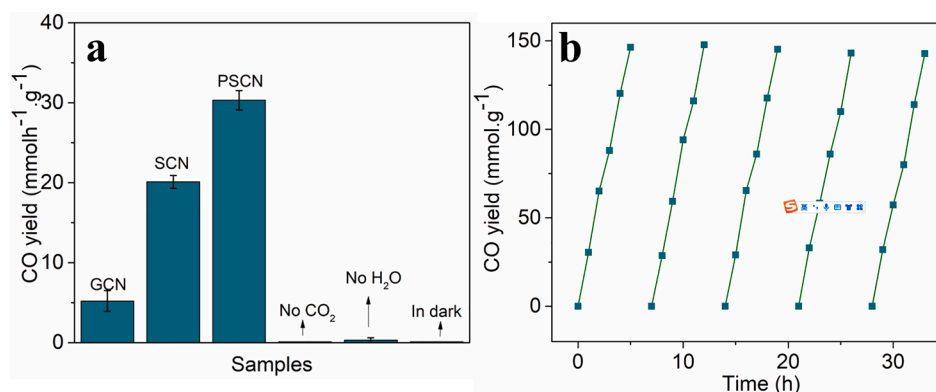


Fig. 9. Photocatalytic CO_2 reduction of GCN, SCN, and PSCN (a); Photocatalytic stability test of PSCN (b).

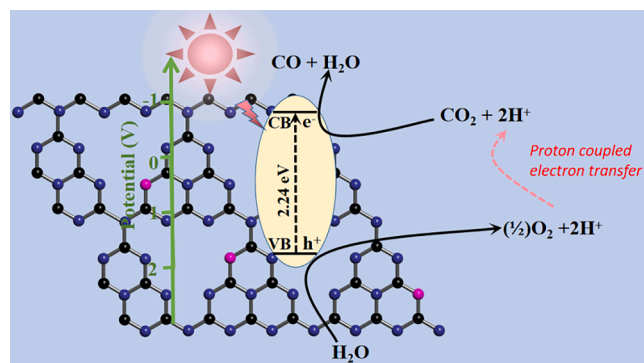
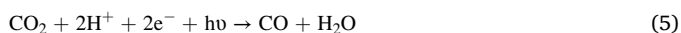
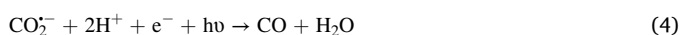


Fig. 10. Possible photocatalytic CO₂ reduction mechanism for CO production.

and 1.5 times, respectively. As seen in Fig. 9b, the PSCN catalyst's photocatalytic CO₂ reduction activity was studied under conditions of sustained visible light illumination. The catalyst's activity after 5 cycles of reactions did not exhibit a significant decline in photocatalytic activity, confirming that PSCN was stable and had a long service life. It's noteworthy that no other products like CH₃OH or CH₄ generated by the photocatalyst were detected by gas chromatography (Fig. 10).

3.5. Photocatalytic mechanism.

Generally, the photocatalytic CO₂ reduction reaction involves the following three steps: (i) CO₂ adsorption and activation; (ii) photo-produced charge carriers excitation and transfer to the catalyst surface; and (iii) photocatalytic reaction [55]. Upon illumination with light, the photocatalyst generated electrons (e⁻) in the CB and holes (h⁺) in the VB, as shown in Eq. (1). Further, The e⁻ are exploited to reduce CO₂ to its radical (CO₂⁻), as shown in Eq. (2) [35]. The water (H₂O) oxidation arises at VB of the catalyst to produce the energetic protons (H⁺) and oxygen (Eq. 3). The CO₂⁻, H⁺ and e⁻ further boosted the rate of CO generation (Eq. 4), which involves a 2e⁻/2H⁺ reduction process [56] as shown in Eq. (5). In semiconductors, the numerous e⁻ and H⁺ transfer by proton-coupled electron transfer mechanism is feasible for multi e⁻ reduction reaction.



4. Conclusions

In summary, the PSCN photocatalyst was successfully prepared by one-pot hydrothermal synthesis with ultrasonication. The formation of thin ribbon structures and pore channels in PSCN was ascribed to ultrasonic treatment during the synthesis process. The XPS, UV-vis and photocatalytic performance demonstrate that effective S element doping can lower carbon nitride's band gap, minimize free charge carrier recombination, and thus enhance the CO₂ reduction capability under visible light. The photocatalytic CO₂ reduction rate of PSCN reached 30.3 μmol·h⁻¹·g⁻¹, which is 5.8 times that of bulky carbon nitride. This study offers a new method for preparing efficient nonmetal-doped carbon nitride for fuel production and environmental applications.

CRediT authorship contribution statement

Jiabei Wang: Investigation. **Zhiqiang Jiang:** Conceptualization, Data curation, Investigation, Writing – original draft, Writing – review & editing.

Declaration of Competing Interest

The authors declare that they have no known competing financial interests or personal relationships that could have appeared to influence the work reported in this paper.

Acknowledgment

We gratefully acknowledge the funding from the Zhejiang Province Basic Public Welfare Research Program (LGG22E080012) and Zhejiang Institute of Tianjin University (ZITJU2022-ZYHY017, ZITJU2022-ZYHY011).

References

- [1] C.M. Jens, L. Müller, K. Leonhard, A. Bardow, To integrate or not to integrate—techno-economic and life cycle assessment of CO₂ capture and conversion to methyl formate using methanol, *ACS Sustain. Chem. Eng.* 7 (2019) 12270–12280.
- [2] Q. Jiang, Z. Chen, J. Tong, M. Yang, Z. Jiang, C. Li, Catalytic Function of IrOx in the Two-Step Thermochemical CO₂-Splitting Reaction at High Temperatures, *ACS Catal.* 6 (2016) 1172–1180.
- [3] Y. Nian, Y. Wang, A.N. Biswas, X. Chen, Y. Han, J.G. Chen, Trends and descriptors for tuning CO₂ electroreduction to synthesis gas over Ag and Au supported on transition metal carbides and nitrides, *Chem. Eng. J.* 426 (2021), 130781.
- [4] Y. Xia, Z. Tian, T. Heil, A. Meng, B. Cheng, S. Cao, J. Yu, M. Antonietti, Highly Selective CO₂ Capture and Its Direct Photochemical Conversion on Ordered 2D/1D Heterojunctions, *Joule* 3 (2019) 2792–2805.
- [5] N. Li, R. Jiang, Y. Li, J. Zhou, Q. Ma, S. Shen, M. Liu, Plasma-Assisted Photocatalysis of CH₄ and CO₂ into Ethylene, *ACS Sustain. Chem. Eng.* 7 (2019) 11455–11463.
- [6] I.S. Pieta, B. Gieroba, G. Kalisz, P. Pieta, R. Nowakowski, M. Naushad, A. Rath, M. B. Gawande, A. Sroka-Bartnicka, R. Zboril, Developing benign Ni/g-C₃N₄ catalysts for CO₂ hydrogenation: activity and toxicity study, *Ind. Eng. Chem. Res.* 61 (2022) 10496–10510.
- [7] F.-X. Shen, J. Shi, T.-Y. Chen, F. Shi, Q.-Y. Li, J.-Z. Zhen, Y.-F. Li, Y.-N. Dai, B. Yang, T. Qu, Electrochemical reduction of CO₂ to CO over Zn in propylene carbonate/tetrabutylammonium perchlorate, *J. Power Sources* 378 (2018) 555–561.
- [8] M. Mousavi, A. Habibi-Yangjeh, S.R. Pouran, Review on magnetically separable graphitic carbon nitride-based nanocomposites as promising visible-light-driven photocatalysts, *J. Mater. Sci. Mater. Electron.* 29 (2018) 1719–1747.
- [9] K. Qi, S.-Y. Liu, A. Zada, Graphitic carbon nitride, a polymer photocatalyst, *J. Taiwan Inst. Chem. Eng.* 109 (2020) 111–123.
- [10] J. Fu, K. Jiang, X. Qiu, J. Yu, M. Liu, Product selectivity of photocatalytic CO₂ reduction reactions, *Mater. Today* 32 (2020) 222–243.
- [11] P. Singh, R.K. Yadav, K. Kumar, Y. Lee, A.K. Gupta, K. Kumar, B.C. Yadav, S. N. Singh, D.K. Dwivedi, S.-H. Nam, A.P. Singh, T.W. Kim, Eosin-Y and sulfur-doped g-C₃N₄ composite for photocatalytic applications: the regeneration of NADH/NADPH and the oxidation of sulfide to sulfoxide, *Catalysis, Sci. Technol.* 11 (2021) 6401–6410.
- [12] K. Qi, N. Cui, M. Zhang, Y. Ma, G. Wang, Z. Zhao, A. Khataee, Ionic liquid-assisted synthesis of porous boron-doped graphitic carbon nitride for photocatalytic hydrogen production, *Chemosphere* 272 (2021), 129953.
- [13] D. Chen, K. Wang, T. Ren, H. Ding, Y. Zhu, Synthesis and characterization of the ZnO/mpg-C₃N₄ heterojunction photocatalyst with enhanced visible light photoactivity, *Dalton Trans.* 43 (2014) 13105–13114.
- [14] S.-Y. Liu, A. Zada, X. Yu, F. Liu, G. Jin, NiFe₂O₄/g-C₃N₄ heterostructure with an enhanced ability for photocatalytic degradation of tetracycline hydrochloride and antibacterial performance, *Chemosphere* 307 (2022), 135717.
- [15] J. Yu, K. Wang, W. Xiao, B. Cheng, Photocatalytic reduction of CO₂ into hydrocarbon solar fuels over g-C₃N₄-Pt nanocomposite photocatalysts, *PCCP* 16 (2014) 11492–11501.
- [16] F. He, B. Zhu, B. Cheng, J. Yu, W. Ho, W. Macyk, 2D/2D/0D TiO₂/C₃N₄/Ti₃C₂ MXene composite S-scheme photocatalyst with enhanced CO₂ reduction activity, *Appl Catal B* 272 (2020), 119006.
- [17] K. Dziadek, W. Waclawek, Metals in the environment, Part I. Heavy metals (Zn, Cu, Ni, Pb, Cd) in the soil environment, *Chemia, Dydaktyka, Ekologia, Metrologia* 10 (2005) 33–44.
- [18] S.-Y. Liu, J. Ru, F. Liu, NiP/CuO composites: Electroless plating synthesis, antibiotic photodegradation and antibacterial properties, *Chemosphere* 267 (2021), 129220.
- [19] W. Chen, D. Jiang, M. Zhu, T. Shi, H. Li, K. Wang, An effective strategy for fabricating highly dispersed nanoparticles on O-C₃N₄ with enhanced electrocatalytic activity and stability, *J. Alloy. Compd.* 741 (2018) 1203–1211.

- [20] E.B. Chubenko, A.V. Baglov, M.S. Leonenya, G.P. Yablonskii, V.E. Borisenko, Structure of Photoluminescence Spectra of Oxygen-Doped Graphitic Carbon Nitride, *J. Appl. Spectrosc.* 87 (2020) 9–14.
- [21] D.R. Miller, D.C. Swenson, E.G. Gillan, Synthesis and structure of 2,5,8-triazido-s-heptazine: an energetic and luminescent precursor to nitrogen-rich carbon nitrides, *J. Am. Chem. Soc.* 126 (2004) 5372–5373.
- [22] E.G. Gillan, Synthesis of nitrogen-rich carbon nitride networks from an energetic molecular azide precursor, *Chem. Mater.* 12 (2000) 3906–3912.
- [23] J. Fang, H. Fan, M. Li, C. Long, Nitrogen self-doped graphitic carbon nitride as efficient visible light photocatalyst for hydrogen evolution, *J. Mater. Chem. A* 3 (2015) 13819–13826.
- [24] A. Chatzoudis, V. Giannopoulos, F. Hollmann, I. Smonou, Surface-doped graphitic carbon nitride catalyzed photooxidation of olefins and dienes: chemical evidence for electron transfer and singlet oxygen mechanisms, *Catalysts* 9 (2019) 639.
- [25] P. Deng, H. Li, Z. Wang, Y. Hou, Enhanced photocatalytic hydrogen evolution by carbon-doped carbon nitride synthesized via the assistance of cellulose, *Appl. Surf. Sci.* 504 (2020), 144454.
- [26] J. Ran, W. Guo, H. Wang, B. Zhu, J. Yu, S.-Z. Qiao, Metal-Free 2D/2D phosphorene/g-C₃N₄ Van der Waals heterojunction for highly enhanced visible-light photocatalytic H₂ production, *Adv. Mater.* 30 (2018) 1800128.
- [27] B. Chai, J. Yan, C. Wang, Z. Ren, Y. Zhu, Enhanced visible light photocatalytic degradation of Rhodamine B over phosphorus doped graphitic carbon nitride, *Appl. Surf. Sci.* 391 (2017) 376–383.
- [28] G. Liu, P. Niu, C. Sun, S.C. Smith, Z. Chen, G.Q. Lu, H.-M. Cheng, Unique Electronic Structure Induced High Photoreactivity of Sulfur-Doped Graphitic C₃N₄, *J. Am. Chem. Soc.* 132 (2010) 11642–11648.
- [29] K. Wang, Q. Li, B. Liu, B. Cheng, W. Ho, J. Yu, Sulfur-doped g-C₃N₄ with enhanced photocatalytic CO₂-reduction performance, *Appl Catal B* 176–177 (2015) 44–52.
- [30] L.J. Fang, Y.H. Li, P.F. Liu, D.P. Wang, H.D. Zeng, X.L. Wang, H.G. Yang, Facile fabrication of large-aspect-ratio g-C₃N₄ nanosheets for enhanced photocatalytic hydrogen evolution, *ACS Sustain. Chem. Eng.* 5 (2017) 2039–2043.
- [31] B. Liu, L. Ye, R. Wang, J. Yang, Y. Zhang, R. Guan, L. Tian, X. Chen, Phosphorus-doped graphitic carbon nitride nanotubes with amino-rich surface for efficient CO₂ capture, enhanced photocatalytic activity, and product selectivity, *ACS Appl. Mater. Interfaces* 10 (2018) 4001–4009.
- [32] S. Bai, N. Zhang, C. Gao, Y. Xiong, Defect engineering in photocatalytic materials, *Nano Energy* 53 (2018) 296–336.
- [33] Y. Xiao, G. Tian, W. Li, Y. Xie, B. Jiang, C. Tian, D. Zhao, H. Fu, Molecule self-assembly synthesis of porous few-layer carbon nitride for highly efficient photoredox catalysis, *J. Am. Chem. Soc.* 141 (2019) 2508–2515.
- [34] J. Cui, D. Qi, X. Wang, Research on the techniques of ultrasound-assisted liquid-phase peeling, thermal oxidation peeling and acid-base chemical peeling for ultrathin graphite carbon nitride nanosheets, *Ultrasonics Sonochemistry* 48 (2018) 181–187.
- [35] S. Bhowmik, S.J. Phukan, N.K. Sah, M. Roy, S. Garai, P.K. Iyer, Review of graphitic carbon nitride and its composite catalysts for selective reduction of CO₂, *ACS Applied Nano Materials* 4 (2021) 12845–12890.
- [36] Z. Jiang, Y. Shen, Y. You, Synthesis of porous carbon nitride nanobelts for efficient photocatalytic reduction of CO₂, *Molecules* 27 (2022) 6054.
- [37] J. Pampel, A. Mehmood, M. Antonietti, T.P. Feller, Ionothermal template transformations for preparation of tubular porous nitrogen doped carbons, *Mater. Horiz.* 4 (2017) 493–501.
- [38] F. Dong, Z. Wang, Y. Sun, W.-K. Ho, H. Zhang, Engineering the nanoarchitecture and texture of polymeric carbon nitride semiconductor for enhanced visible light photocatalytic activity, *J. Colloid Interface Sci.* 401 (2013) 70–79.
- [39] Y. Zhang, J. Liu, G. Wu, W. Chen, Porous graphitic carbon nitride synthesized via direct polymerization of urea for efficient sunlight-driven photocatalytic hydrogen production, *Nanoscale* 4 (2012) 5300–5303.
- [40] J. Liu, T. Zhang, Z. Wang, G. Dawson, W. Chen, Simple pyrolysis of urea into graphitic carbon nitride with recyclable adsorption and photocatalytic activity, *J. Mater. Chem.* 21 (2011) 14398–14401.
- [41] R. You, H. Dou, L. Chen, S. Zheng, Y. Zhang, Graphitic carbon nitride with S and O codoping for enhanced visible light photocatalytic performance, *RSC Adv.* 7 (2017) 15842–15850.
- [42] P. Chen, B. Lei, X.A. Dong, H. Wang, J. Sheng, W. Cui, J. Li, Y. Sun, Z. Wang, F. Dong, Rare-earth single-atom La–N charge-transfer bridge on carbon nitride for highly efficient and selective photocatalytic CO₂ reduction, *ACS Nano* 14 (2020) 15841–15852.
- [43] L. Chen, Y. Man, Z. Chen, Y. Zhang, Ag/g-C₃N₄/N₄-layered composites with enhanced visible light photocatalytic performance, *Mater. Res. Express* 3 (2016), 115003.
- [44] D. Gao, Y. Liu, P. Liu, M. Si, D. Xue, Atomically thin B doped g-C₃N₄ Nanosheets: High-Temperature Ferromagnetism and calculated Half-Metallicity, *Sci. Rep.* 6 (2016) 35768.
- [45] J. Yu, S. Wang, B. Cheng, Z. Lin, F. Huang, Noble metal-free Ni(OH)₂-g-C₃N₄ composite photocatalyst with enhanced visible-light photocatalytic H₂-production activity, *Catalysis, Sci. Technol.* 3 (2013) 1782–1789.
- [46] Q. Liang, M. Zhang, C. Liu, S. Xu, Z. Li, Sulfur-doped graphitic carbon nitride decorated with zinc phthalocyanines towards highly stable and efficient photocatalysis, *Appl. Catal. A* 519 (2016) 107–115.
- [47] X. Bai, M. Li, J. Li, X. Rao, S. Zheng, Y. Zhang, Graphitic Carbon Nitride Codoped with Sulfur and Yttrium for Efficient Visible-Light Photocatalytic Performance, *ACS Applied Energy Materials* 4 (2021) 14390–14399.
- [48] Y. Huang, D. Li, Z. Fang, R. Chen, B. Luo, W. Shi, Controlling carbon self-doping site of g-C₃N₄ for highly enhanced visible-light-driven hydrogen evolution, *Appl Catal B* 254 (2019) 128–134.
- [49] W. Iqbal, B. Qiu, J. Lei, L. Wang, J. Zhang, M. Anpo, One-step large-scale highly active g-C₃N₄ nanosheets for efficient sunlight-driven photocatalytic hydrogen production, *Dalton Trans.* 46 (2017) 10678–10684.
- [50] N. Tian, Y. Zhang, X. Li, K. Xiao, X. Du, F. Dong, G.I.N. Waterhouse, T. Zhang, H. Huang, Precursor-reforming protocol to 3D mesoporous g-C₃N₄ established by ultrathin self-doped nanosheets for superior hydrogen evolution, *Nano Energy* 38 (2017) 72–81.
- [51] Y. Zhou, W. Lv, B. Zhu, F. Tong, J. Pan, J. Bai, Q. Zhou, H. Qin, Template-free one-step synthesis of g-C₃N₄ nanosheets with simultaneous porous network and S-doping for remarkable visible-light-driven hydrogen evolution, *ACS Sustain. Chem. Eng.* 7 (2019) 5801–5807.
- [52] G. Dong, Y. Zhang, Q. Pan, J. Qiu, A fantastic graphitic carbon nitride (g-C₃N₄) material: Electronic structure, photocatalytic and photoelectronic properties, *J. Photochem Photobiol C: Photochem Rev* 20 (2014) 33–50.
- [53] Y. Zhang, Q. Pan, G. Chai, M. Liang, G. Dong, Q. Zhang, J. Qiu, Synthesis and luminescence mechanism of multicolor-emitting g-C₃N₄ nanopowders by low temperature thermal condensation of melamine, *Sci. Rep.* 3 (2013).
- [54] K. Qi, W. Lv, I. Khan, S.-Y. Liu, Photocatalytic H₂ generation via CoP quantum-dot-modified g-C₃N₄ synthesized by electroless plating, *Chin. J. Catal.* 41 (2020) 114–121.
- [55] S. Huang, H. Yi, L. Zhang, Z. Jin, Y. Long, Y. Zhang, Q. Liao, J. Na, H. Cui, S. Ruan, Y. Yamauchi, T. Wakihara, Y.V. Kaneti, Y.-J. Zeng, Non-precious molybdenum nanospheres as a novel cocatalyst for full-spectrum-driven photocatalytic CO₂ reforming to CH₄, *J. Hazard. Mater.* 393 (2020), 122324.
- [56] J. Hong, W. Zhang, J. Ren, R. Xu, Photocatalytic reduction of CO₂: a brief review on product analysis and systematic methods, *Anal. Methods* 5 (2013) 1086–1097.